

# Variability of the UV luminosity function with SPICE

Arghyadeep Basu <sup>1,2\*</sup>, Aniket Bhagwat <sup>1</sup>, Benedetta Ciardi <sup>1</sup> & Tiago Costa <sup>3</sup>

<sup>1</sup>Max-planck-Institut für Astrophysik, Karl-Schwarzschild-Strasse 1, D-85741, Garching, Germany

<sup>2</sup>Ludwig-Maximilians-Universität München (LMU), Geschwister-Scholl-Platz 1, 80539 München, Germany

<sup>3</sup>School of Mathematics, Statistics and Physics, Newcastle University, NE1 7RU, UK

Accepted XXX. Received YYY; in original form ZZZ

## ABSTRACT

We investigate the variability of the UV luminosity function (UVLF) at  $z > 5$  using the SPICE suite of cosmological, radiation-hydrodynamic simulations, which include three distinct supernova (SN) feedback models: *bursty-sn*, *smooth-sn*, and *hyper-sn*. The *bursty-sn* model, driven by intense and episodic SN explosions, produces the highest fluctuations in the star formation rate (SFR). Conversely, the *smooth-sn* model, characterized by gentler SN feedback, results in minimal SFR variability. The *hyper-sn* model, featuring a more realistic prescription that incorporates hypernova (HN) explosions, exhibits intermediate variability, closely aligning with the *smooth-sn* trend at lower redshifts. These fluctuations in SFR significantly affect the  $M_{UV} - M_{halo}$  relation, a proxy for UVLF variability. Among the models, *bursty-sn* produces the highest UVLF variability, with a maximum value of 2.5. In contrast, the *smooth-sn* and *hyper-sn* models show substantially lower variability, with maximum values of 1.3 and 1.5, respectively. However, in all cases, UVLF variability strongly correlates with host halo mass, with lower-mass halos showing greater variability due to more effective SN feedback in their shallower gravitational wells. The *bursty-sn* model, though, results in higher amplitudes. Variability decreases in lower mass haloes with decreasing redshift for all feedback models. This study underscores the critical role of SN feedback in shaping the UVLF, and highlights the mass and redshift dependence of its variability, suggesting that UVLF variability may alleviate the bright galaxy tension observed by JWST at high redshifts.

**Key words:** galaxies: formation – galaxies: luminosity function, mass function – galaxies: star formation – galaxies: high-redshift

## 1 INTRODUCTION

Since the James Webb Space Telescope (JWST) started to provide revolutionary data in July 2022, our understanding of the early galaxy formation process has been challenged. Although over the past decade the Hubble Space Telescope (HST) enabled us to observe galaxies out to  $z \approx 10$  (Zheng et al. 2012; Coe et al. 2013; Oesch et al. 2016; Morishita et al. 2018; Bagley et al. 2022), JWST has pushed our observational barrier to even higher redshifts, and has detected an unexpected overabundance of massive galaxies at  $z > 10$  (Castellano et al. 2022; Finkelstein et al. 2022; Naidu et al. 2022; Adams et al. 2023; Morishita & Stiavelli 2023; Bouwens et al. 2023a,b; Donnan et al. 2023a; Atek et al. 2023; Pérez-González et al. 2023; Willott et al. 2024; Donnan et al. 2024). This discovery might challenge theoretical models, as it suggests a high incidence of bright galaxies at this epoch (Mason et al. 2023; Boylan-Kolchin 2023; Lovell et al. 2023; Acharya et al. 2024). The recent detection of a spectroscopically confirmed galaxy at  $z = 14.32$  by Helton et al. (2024) significantly elevates the challenge, suggesting that such bright objects exist even at these high redshifts. These observations raise several intriguing questions: Could there be a missing population of bright stars? Is there something unique about the early star formation history? Do these findings create tensions with the standard  $\Lambda$ CDM cosmology?

A few potential physical processes have been suggested to explain the discovery of these bright galaxies. One of them is an increased star formation efficiency (SFE) due to a weaker feedback which could boost the abundance of UV-bright galaxies by forming more stars per baryon (Fukushima & Yajima 2022; Inayoshi et al. 2022; Harikane et al. 2023). Also, a top-heavy initial mass function (IMF) could lead to an abundance of early bright galaxies by producing more UV photons per unit of stellar mass formed (Inayoshi et al. 2022; Yung et al. 2023; Chon et al. 2024; Steinhardt et al. 2023; Cueto et al. 2024; Hutter et al. 2024). The interplay between dust attenuation and the abundance of massive halos at high redshifts could lead to a mild evolution of the UV luminosity function (LF). While this alone cannot fully explain the abundance of high-redshift bright galaxies (Ferrara et al. 2023; Mirocha & Furlanetto 2023), radiation pressure on dust may contribute to the reduction of the attenuation (Fiore et al. 2023; Ferrara et al. 2024). More exotic scenarios invoked include a modified primordial power spectrum (Hirano & Yoshida 2023; Padmanabhan & Loeb 2023; Parashari & Laha 2023; Sabti et al. 2023), primordial non-Gaussianity (Biagetti et al. 2023), and alternative dark matter scenarios (Bird et al. 2023; Dayal & Giri 2023; Gong et al. 2023). In this respect, though, it is important to acknowledge several key factors that may influence these observations. For instance, spectral energy distribution (SED) fitting methods often carry significant uncertainties (Lower et al. 2020; Hollis 2023; Jain et al. 2024; Haskell et al. 2024). Additionally, observational biases,

\* E-mail: basu@mpa-garching.mpg.de

the potential misinterpretation of field overdensities, and challenges in making proper comparisons to simulations may further complicate the understanding of early bright galaxy populations (Narayanan et al. 2024; Luberto et al. 2024; Nguyen et al. 2024; Whitler et al. 2024).

Another topic that has attracted significant attention is the variability of the UVLF of early galaxies. A possible explanation for its origin is a strong stochasticity of star formation. Indeed, both simulations and observations indicate that small dwarf galaxies and high-redshift galaxies display stochastic star formation histories (Sparre et al. 2017; Smit et al. 2016; Emami et al. 2019; Iyer et al. 2020; Tacchella et al. 2020; Flores Velázquez et al. 2021; Hopkins et al. 2023), which are also associated to irregular and clumpy morphologies of the hosting galaxies (Bournaud et al. 2007; Elmegreen et al. 2009; Förster Schreiber et al. 2011; Treu et al. 2023). The variability in star formation efficiency is likely driven by a combination of factors, including gas inflow and outflow dynamics, gravitational instabilities, and galaxy mergers during the early stages of galaxy formation (Dekel et al. 2009; Ceverino et al. 2010; Anglés-Alcázar et al. 2017), intense feedback (El-Badry et al. 2016; Tacchella et al. 2016) or sometimes even feedback-free starbursts (Faucher-Giguère 2018; Dekel et al. 2023). These combined effects alter the galactic environment, leading to variability in the UVLF (Sparre et al. 2017; Furlanetto & Mirocha 2022; Sun et al. 2023b).

In this paper, we investigate the impact of SFR variability on the UVLF of high- $z$  galaxies using the suite of radiation hydrodynamic simulations SPICE (Bhagwat et al. 2024, hereafter B24), which comprises three different implementations of supernova (SN) feedback (while the rest of the simulation setup is the same), resulting in a different level of burstiness and in a variety of star formation histories. This allows us to systematically quantify the SFR and UVLF variability.

Specifically, we introduce the simulations in Section 2, the results are presented in Section 3, while in Section 4 we summarise our conclusions and future prospects. Throughout the paper, we adopt a flat  $\Lambda$ CDM cosmology consistent with Planck Collaboration et al. (2016) with  $\Omega_m = 0.3099$ ,  $\Omega_\Lambda = 0.6901$ ,  $\Omega_b = 0.0489$ ,  $h = 0.6774$ ,  $\sigma_8 = 0.8159$  and  $n_s = 0.9682$ , where the symbols have their usual meaning.

## 2 THE SPICE SIMULATION SUITE

In order to investigate the impact of SN feedback onto galaxy properties, we post-process the suite of radiation-hydrodynamical simulations SPICE (B24), which we briefly introduce below.

SPICE has been performed with RAMSES-RT (Rosdahl et al. 2013; Rosdahl & Teyssier 2015), the radiation-hydrodynamics extension of the Eulerian Adaptive Mesh Refinement (AMR) code RAMSES (Teyssier 2002). The simulations target a cubic box of size  $10 h^{-1} \text{cMpc}$  with  $512^3$  dark matter particles of mean mass  $m_{\text{dm}} = 6.38 \times 10^5 M_\odot$ . The AMR allows each parent gas cell to split into 8 smaller cells when certain conditions are met (see B24). As a reference, this provides a physical resolution at  $z = 5$  ranging from 4.8 kpc for the coarsest level ( $\ell_{\text{min}} = 9$ ) to approximately 28 pc for the finest level ( $\ell_{\text{max}} = 16$ ). The hydrodynamical equations are solved using a second order Godonov scheme and the dynamics of collisionless dark matter and stellar particles are computed by solving the Poisson equation with a particle-mesh solver, projecting onto a grid using the Cloud-in-Cell scheme (Guillet & Teyssier 2011). Gas cooling and heating are accounted for as in Rosdahl et al. (2013). Star-formation has been modelled following Kretschmer & Teyssier

(2020), which adopt a subgrid turbulence model depending on the physical conditions of each computational cell including parameters like the local gas turbulent Mach number and the virial parameter, which acts as a measure of the gravitational balance in the region, and which results in a spatially-variable star formation efficiency. Additionally, SPICE includes a radiative transfer scheme with five frequency groups, i.e. infrared (0.1-1 eV), optical (1-13.6 eV), and three UV (13.6-24.59 eV; 24.59-54.42 eV; 54.42- $\infty$  eV).

To correctly capture the momentum injection into the cells due to supernova feedback, the scheme presented in Kimm et al. (2015) is adopted. Keeping all the parameters for momentum injection constant, different simulations have been run based on the timing of supernova events and the amount of energy injected. We briefly present the different feedback models as follows:

- **"bursty-sn"**: each stellar particle experiences a single event of SN explosions at a fixed timescale of 10 Myr, equivalent to the mean time at which SN occurs for the adopted Chabrier (2003) initial mass function. An energy of  $2 \times 10^{51}$  ergs per SN explosion is injected into the neighbouring cells.

- **"smooth-sn"**: for a given stellar population, a SN with mass  $> 20M_\odot$  can explode as early as 3 Myr, whereas SN with progenitor mass of  $8M_\odot$  can explode as late as 40 Myr. An energy of  $2 \times 10^{51}$  ergs per SN explosion is injected into the neighbouring cells.

- **"hyper-sn"**: SN explosions happen at different times as in smooth-sn, with the injected energy extracted stochastically from a normal distribution centered at  $1.2 \times 10^{51}$  ergs and ranging from  $10^{50}$  ergs to  $2 \times 10^{51}$  ergs (see also, Sukhbold et al. 2016; Díaz-Rodríguez et al. 2018, 2021). Additionally, a metallicity dependent fraction of SN explodes as Hypernovae (HN), with an energy injection of  $10^{52}$  ergs.

Dust in SPICE is not modelled as an active ingredient but rather through a direct dependence on the local gas-phase properties, i.e. its metallicity and ionization state. Following Nickerson et al. (2018), the dust number density is computed as  $n_d = (Z/Z_\odot) f_d n_H$ , where  $Z$  represents the local metallicity,  $f_d = 1 - x_{\text{HII}}$  is the fraction of neutral hydrogen, and  $n_H$  is the hydrogen number density. This relation ensures that the dust density depends on both chemical enrichment and the local ionization conditions. Indeed, despite expectations of dust being typically destroyed in photo-ionized gas, observations have shown dust-to-ionized-gas ratios as high as 0.01 (Harper & Low 1971; Contini & Contini 2003; Laursen et al. 2009). Thus, the quantity  $f_d$  permits non-zero dust effects even in partially ionized environments. The propagation of UV photons influences the gas via photo-ionization and photo-heating, but also through radiation pressure generated from both photo-ionization and through dust absorption. Infrared and optical photons interact with gas solely through radiation pressure on dust particles. Each photon group is characterized by specific dust absorption and scattering properties. When optical and UV photons are absorbed by dust, their energy is transferred to the infrared group, which later interacts with the gas through multi-scattering radiation pressure.

For a more comprehensive description of the simulations and the supernova feedback models discussed above, we refer the readers to B24.

## 3 RESULTS

In this Section, we present results from our analysis of how different SN feedback models affect the SFR and UVLF.

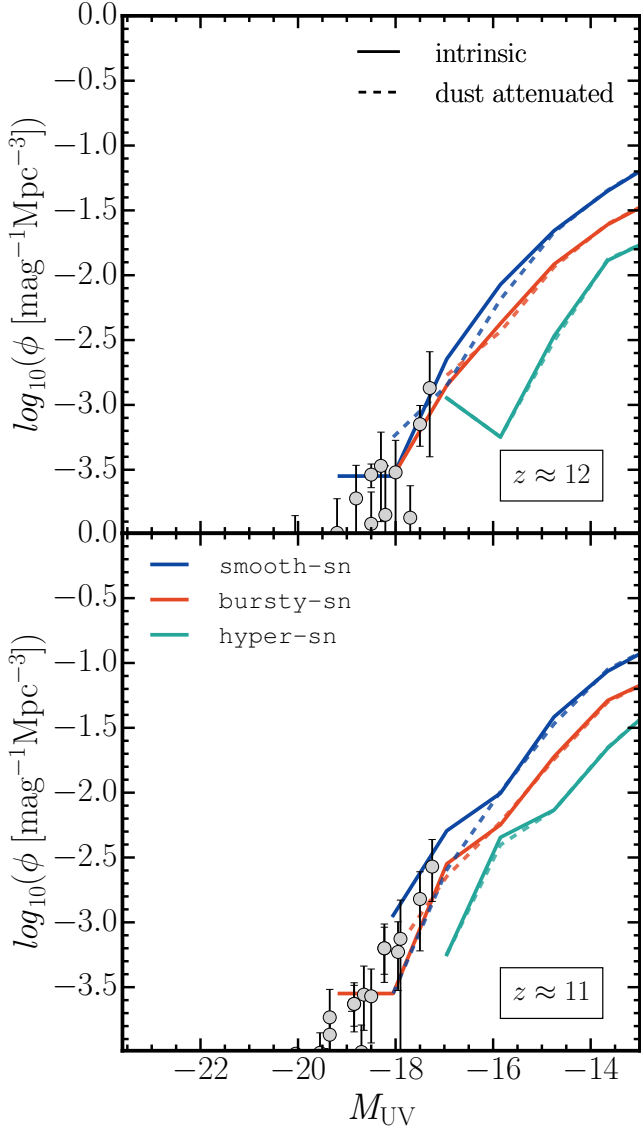


**Figure 1.** 1500 Å luminosity functions at  $z = 12$  (top panel) and 11 (bottom panel) for three feedback models (in different colors). Solid and dashed curves refer to intrinsic and dust attenuated LFs, respectively. A compilation of observations from HST and JWST (Bouwens et al. 2015; Harikane et al. 2022; Naidu et al. 2022; Adams et al. 2023; Harikane et al. 2023; Bouwens et al. 2023a,b; Leung et al. 2023; Donnan et al. 2023b,c; Pérez-González et al. 2023; Casey et al. 2024; Robertson et al. 2024; McLeod et al. 2024; Whitler et al. 2025) is shown as gray data points.

### 3.1 UV luminosity function

While in B24 we showed results at  $z \leq 10$ , in Figure 1 we present the 1500 Å LF for all feedback models at  $z = 11$  and 12. The LFs have been derived from the stellar spectral energy distribution within a 10 Å bin centered around 1500 Å. We use the SED model of BPASSv2.2.1 (Eldridge et al. 2017; Stanway & Eldridge 2018), assuming the Chabrier (2003) IMF (details are mentioned in B24). The solid and dashed lines in the figure indicate the intrinsic and dust-attenuated luminosity functions, respectively. To account for dust attenuation, we utilize the Monte Carlo radiative transfer code RASCAS (Michel-Dansac et al. 2020). In this approach, 100 rays are

cast from each stellar particle within a halo out to its virial radius. The dust attenuation along each ray is computed following the model described in the previous section.

As already noted in B24, also at these redshifts smooth-sn produces a higher intrinsic luminosity function (by 0.3-0.4 dex) at all magnitudes. Conversely, the hyper-sn model yields the lowest galaxy count across all magnitude bins. The bursty-sn model produces results which are typically in between those of the other models. The effect of dust attenuation (dashed curves) starts to be visible from an absolute magnitude of  $M_{1500} \approx -15$ , the value changing slightly depending on feedback model and redshift. When comparing the dust attenuated LFs to a compilation of observations from HST and JWST (Bouwens et al. 2015; Harikane et al. 2022; Naidu et al. 2022; Adams et al. 2023; Harikane et al. 2023; Bouwens et al. 2023a,b; Leung et al. 2023; Donnan et al. 2023b,c; Pérez-González et al. 2023; Casey et al. 2024; Robertson et al. 2024; McLeod et al. 2024; Whitler et al. 2025), we notice a fairly good match in the range of magnitudes covered by SPICE (except for the hyper-sn model), which, given the limited box size, does not extend to the brightest observed galaxies. However, to assess whether the extrapolated UVLF aligns with observations, we parametrize and fit the curves using the commonly adopted Schechter (1976) function (see Appendix B). For a more detailed discussion of the LF, we refer the reader to B24.

In Figure 2, we further investigate the contribution to the bright end of the UVLF (with  $M_{UV}^{\text{dust}} \leq -17$ ) from objects with different stellar masses. To obtain a statistical sample, we have derived the distributions using all the simulation snapshots within a time interval of 100 Myr centered on each redshift shown. We observe that, for all feedback models, the stellar masses are always spread over a wide range, which extends to increasingly larger masses as redshift decreases, indicating that even objects with stellar masses as low as  $10^{(6.5-7)} M_{\odot}$  can contribute to the bright end of the LF. For all models the peak of the distribution drops with time along with the distribution becoming flatter and broader. Notably, though, all models exhibit a similar distribution, although the corresponding medians are slightly different, with smooth-sn, bursty-sn and hyper-sn having the largest median value at  $z \approx 10, 8$  and 6, respectively. For a comparison to previous studies, we also show the stellar mass threshold required for having objects with  $M_{UV}^{\text{dust}} \leq -17$ , obtained in the semi-analytic model of Mason et al. (2015, 2023) (assuming the median SFE model), which has been used to explain the abundance of bright galaxies detected by JWST at  $z > 10$ . It is evident that their estimates are very similar to the median values obtained in our simulations.

To investigate the temporal evolution of the dust-attenuated UVLF on short timescales, in Figure 3 we present the UVLF in intervals of 10, 30 and 50 Myr around  $z \approx 10$  and 8. While the general behaviour in the three models is similar, we find that the UVLF in the bursty-sn model experiences the most pronounced fluctuations, with a deviation of more than 1 dex. In comparison, the smooth-sn model exhibits a more gradual evolution of the UVLF, producing a steady increase in the number of galaxies. As already mentioned in B24, this suggests a smoother star formation process due to the presence of gentler SN feedback. The hyper-sn model shows an intermediate behaviour at  $z \approx 10$ , with variations up to 0.5 dex. At  $z \approx 8$ , the variability in hyper-sn becomes slightly lower than in smooth-sn. In the following sections we will investigate more in detail the origin of such variability.

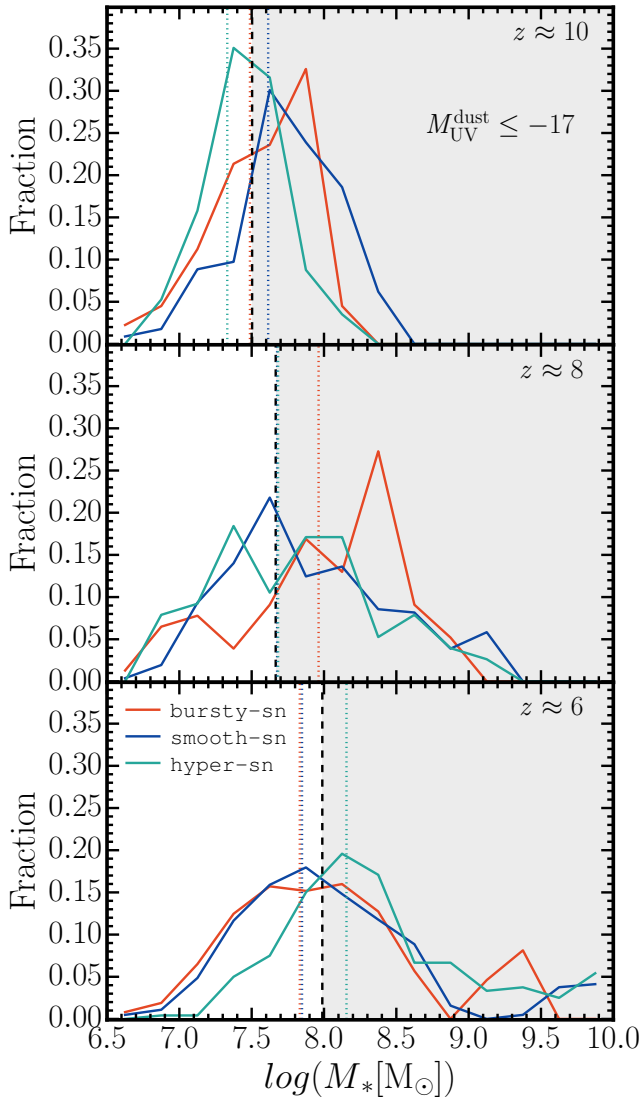


**Figure 2.** Distribution of stellar mass of objects with  $M_{\text{UV}}^{\text{dust}} \leq -17$  at  $z = 10$  (top panel), 8 (middle) and 6 (bottom). The corresponding median stellar masses are shown as vertical dotted lines, while the black dashed lines refer to the minimum stellar mass required for having such bright objects assuming the median SFE model of [Mason et al. \(2015, 2023\)](#).

### 3.2 Star formation rate variability

In this section, we explore how different SN feedback models impact the variability of the SFR. Figure 4 shows the star formation history of the most massive halo from SPICE at  $z = 5$  for the three models. We note that at this redshift the virial mass of the halo is  $2.7 \times 10^{11} M_{\odot}$  and the total stellar mass is  $2.1 \times 10^9 M_{\odot}$ ,  $1.9 \times 10^{10} M_{\odot}$  and  $1.7 \times 10^{10} M_{\odot}$  in the *bursty-sn*, *smooth-sn* and *hyper-sn* model, respectively. It is evident that overall *bursty-sn* produces the largest fluctuations in the SFR, with deviations of up to two orders of magnitude. In contrast, the *smooth-sn* model shows smaller fluctuations. In *hyper-sn*, the SFR is the lowest among the models during the first 200 Myr (i.e. for lookback times larger than 700 Myr), when the impact of HN explosions is the strongest. However, at later times the SFR is similar to that of *smooth-sn*. The fluctuations in *hyper-sn* are comparable to those in *smooth-sn*.

For a more quantitative investigation of the SFR variability, we first

compute the median star-formation main sequence in different halo mass bins and redshift intervals (corresponding to bins of  $100 \text{ Myr}^1$ ),  $\text{SFR}_{\text{median}}$ . In the inset of Figure 4 we show the variability of the SFR for the same halo, defined as  $\delta_{\text{SFR}} = \log_{10}(\text{SFR}/\text{SFR}_{\text{median}})$ , which quantifies how the SFR of the halo deviates from the median SFR computed over the entire sample of halos in the same mass bin. In the inset of Figure 4 we show the distribution of  $\delta_{\text{SFR}}$  for this halo during its entire lifetime, together with the corresponding standard deviation,  $\sigma_{\text{SFR}}$ . As expected, *bursty-sn* shows the widest distribution, with  $\sigma_{\text{SFR, bu}} = 0.34$ , which is more than double the one of *smooth-sn* with  $\sigma_{\text{SFR, sm}} = 0.12$ . *hyper-sn* produces a  $\delta_{\text{SFR}}$  distribution which is similar to the one from *smooth-sn*, with a slightly higher standard deviation of  $\sigma_{\text{SFR, hn}} = 0.14$ , reflecting the stronger fluctuations present at  $z > 9$ .

In Figure 5 we examine the mass dependence of  $\sigma_{\text{SFR}}$  at different redshifts. Typically, smaller halos ( $M_{\text{halo}} < 10^9 M_{\odot}$ ) exhibit a higher degree of variability as compared to more massive ones, suggesting a stronger impact of SN feedback at lower masses. For halos with  $M_{\text{halo}} < 10^9 M_{\odot}$ , all three models have a similar redshift-dependent trend, with the variability decreasing at lower redshifts. However, the *bursty-sn* model consistently shows the highest variability in most redshift bins, whereas *smooth-sn* and *hyper-sn* have a similar behaviour, with the latter showing a slightly higher variability. At  $z < 6$ , all the models become comparable, although *hyper-sn* shows the lowest  $\sigma_{\text{SFR}}$  values. For  $M_{\text{halo}} > 10^{10} M_{\odot}$ , the trend is reversed, i.e. the SFR variability increases as redshift decreases. In *bursty-sn*,  $\sigma_{\text{SFR}}$  remains consistently high and shows little dependence on halo mass at lower redshifts. The behavior of *hyper-sn* mostly mirrors the one of *smooth-sn* except the peak at  $z \approx 5$  for halos with masses around  $10^{10.5} M_{\odot}$ , which reaches the highest SFR variability among all models.

To get an overview of the statistical behaviour of  $\sigma_{\text{SFR}}$ , in Figure 6 we present the distribution of  $\sigma_{\text{SFR}}$  in three halo mass bins:  $M_{\text{halo}} > 10^{10} M_{\odot}$ ,  $10^9 M_{\odot} < M_{\text{halo}} \leq 10^{10} M_{\odot}$ , and  $M_{\text{halo}} \leq 10^9 M_{\odot}$  for the entire redshift range covered in Figure 5. In the *bursty-sn* model, strong and regular fluctuations dominate the overall population, resulting in a  $\sigma_{\text{SFR}}$  distribution skewed towards higher values at all masses in comparison to *smooth-sn*. The *hyper-sn* model produces distributions that typically fall between those of the other two models, although they are much more similar to those of *smooth-sn*. In the highest mass bin, though, *hyper-sn* exhibits a  $\sigma_{\text{SFR}}$  even higher than in *bursty-sn*, which aligns with the pronounced peak observed in Figure 5. For all models, the  $\sigma_{\text{SFR}}$  distributions are wider in the highest mass bin, indicating a broader range of star formation variability. As we move to lower mass halos, the distributions become progressively narrower, indicating a smaller range of variability but centered around higher  $\sigma_{\text{SFR}}$  values. Additionally, as noted earlier in Figure 5, the distributions for all models systematically shift towards higher  $\sigma_{\text{SFR}}$  values as halo mass decreases.

In the following section, we will explore how this mass and redshift-dependent SFR variability influences the variability of the UVLF.

<sup>1</sup> This has been calculated from the SFR values of all the halos present in each 100 Myr time intervals and then computing the median SFR as a function of halo mass. We have also performed the same analysis using bin sizes of 30 and 50 Myr, and found no qualitative differences in our conclusions.



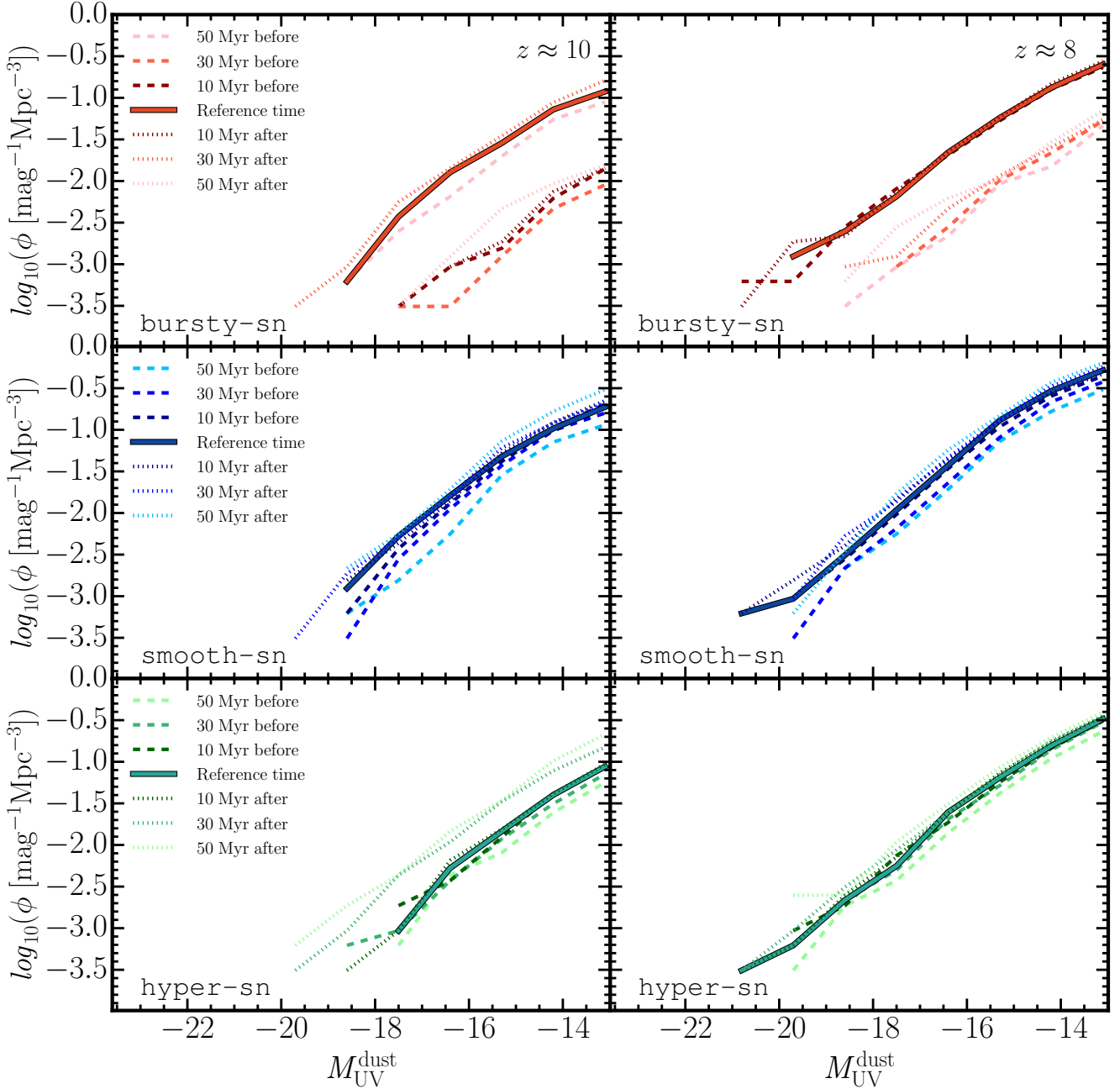


**Figure 3.** Evolution of the dust-attenuated UVLF over time intervals of 10, 30, and 50 Myr (indicated by different color gradients, from dark to light), centered at  $z \approx 10$  (left panel) and 8 (right), for three different feedback models: bursty-sn (top panels), smooth-sn (middle), and hyper-sn (bottom). The dashed and dotted curves show the UVLF before and after the reference time.

### 3.3 Variability of the UV luminosity function

The variability in the UVLF is shaped by three primary factors: the accretion history of galaxies, feedback-regulated star formation histories, and dust attenuation (see Shen et al. 2023). The combined effect of non-linear feedback and accretion history on the SFR is encapsulated in the term  $\sigma_{\text{SFR}}$ , which has been introduced in the previous section. Interstellar medium (ISM) properties (Heckman et al. 2001; Ciardi et al. 2002; Alexandroff et al. 2015), feedback-driven dust destruction and dust distribution within galaxies (Aoyama et al. 2018; Ocvirk et al. 2024; Esmerian & Gnedin 2024; Zhao

& Furlanetto 2024) further influence the escape of UV photons, affecting the observed UVLF.

To examine the variability of the UVLF in SPICE, we compute the scatter in UV luminosity around the median UVLF (see Section 3.1). For a consistent comparison with previous studies, we discuss the variability of the dust-attenuated UVLF ( $\sigma_{\text{UV}}^{\text{dust}}$ ), which generally shows a variability higher than the one of the intrinsic one (Shen et al. 2023; Pallottini & Ferrara 2023). In SPICE, the UVLF variability is influenced by both intrinsic flux fluctuations and dust attenuation, with the former playing a more dominant role. However, in approximately 25 – 35% of cases (with the smooth-sn model

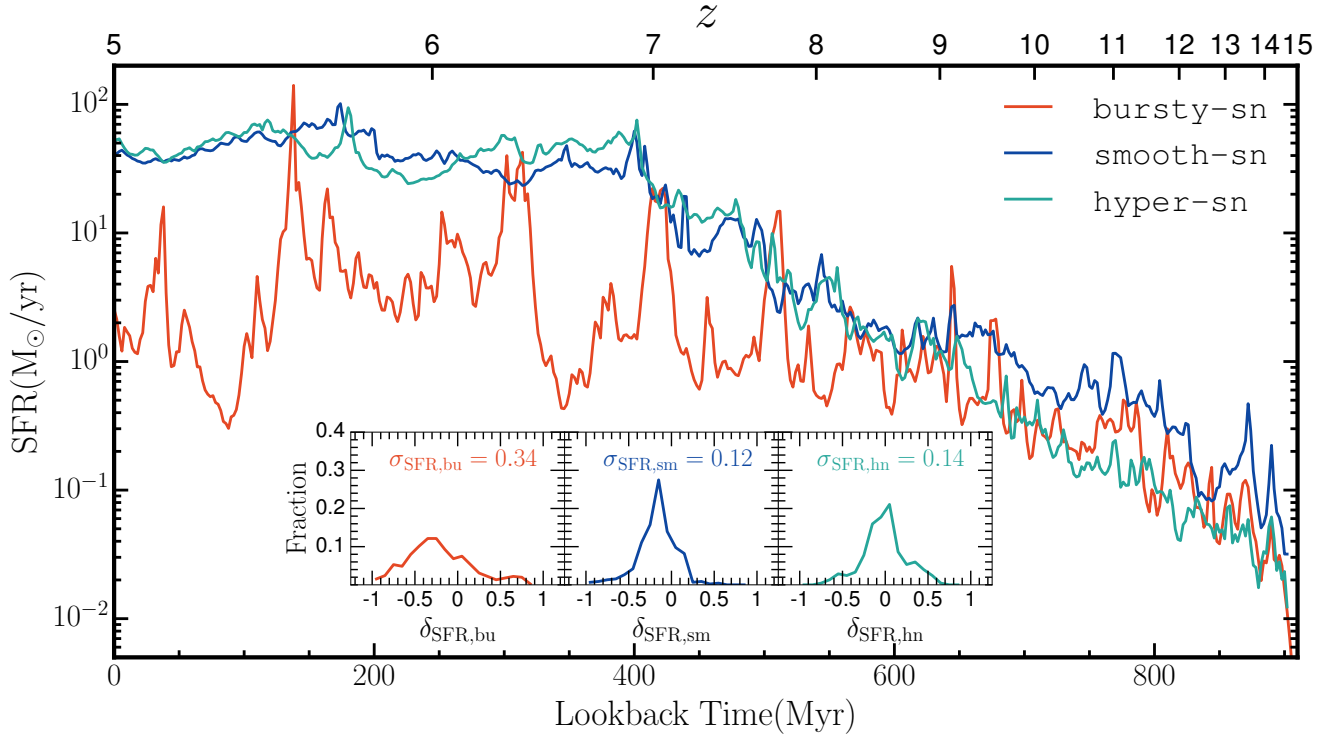


**Figure 4.** Temporal evolution of the SFR averaged over 2 Myr accounting for all stellar particles inside the virial radius of the most massive halo at  $z = 5$ , which has a total stellar mass of  $2.1 \times 10^9 M_\odot$ ,  $1.9 \times 10^{10} M_\odot$  and  $1.7 \times 10^{10} M_\odot$  for the bursty-sn, smooth-sn and hyper-sn model, respectively. Colors refer to the different SN feedback models. In the inset, we show the distributions of  $\delta_{\text{SFR},X}$ , together with the corresponding standard deviation,  $\sigma_{\text{SFR},X}$  (see text for the details of the calculation), where ‘X’ = ‘bu’, ‘sm’, ‘hn’ for the bursty-sn, smooth-sn and hyper-sn model, respectively.

showing the highest fraction), dust attenuation slightly reduces the overall variability of  $\lesssim 4 - 5\%$  with respect to the intrinsic scatter.

Figure 7 shows the scatter in UV luminosity,  $\sigma_{\text{UV}}^{\text{dust}}$ , as a function of  $M_{\text{halo}}$  in the range  $z = 5 - 15$ . At the highest redshifts, all models exhibit a similar dependence on halo mass, with smaller halos showing a larger UVLF variability, likely due to efficient SN feedback in this mass regime (Gelli et al. 2024). As expected, bursty-sn has the highest variability among all models, with a UV luminosity scatter which starts to rise at  $z \lesssim 10$  and reaches  $\sigma_{\text{UV}}^{\text{dust}} \approx 2.5$  for  $M_{\text{halo}} \approx 10^{10.3} M_\odot$  at  $z \approx 6.5$ . At lower redshift,  $\sigma_{\text{UV}}^{\text{dust}}$  decreases again. In comparison, for smooth-sn the UV luminosity scatter is always below  $\sigma_{\text{UV}}^{\text{dust}} \approx 1.3$ , whereas hyper-sn shows slightly higher variability, with a maximum value of  $\sigma_{\text{UV}}^{\text{dust}} \approx 1.5$ . Indeed, hyper-sn exhibits a variability comparable to the one in bursty-sn until  $z \approx 9$ , while at lower redshift the variability decreases as a result of the reduced fraction of HN, and becomes more similar to the smooth-sn one. The same behaviour had already been observed in Figure 4 with respect to the SFR. At  $z < 6$  all models have nearly identical variability levels, except for bursty-sn which shows larger fluctuations, with a maximum deviation up to 0.3-0.4 mag.

Similarly to Figure 6, in Figure 8 we show the distribution of  $\sigma_{\text{UV}}^{\text{dust}}$  in different halo mass bins. As found for the SFR, the curves are shifted towards higher  $\sigma_{\text{UV}}^{\text{dust}}$  for smaller halo masses, with bursty-sn having a broader distribution and the highest peak value overall. smooth-sn and hyper-sn show distributions similar to each other, with the exception of the intermediate mass range (i.e.  $10^9 M_\odot < M_{\text{halo}} \leq 10^{10} M_\odot$ ), where the latter is somewhat wider. In this mass regime, the average  $\sigma_{\text{UV}}^{\text{dust}}$  is about 0.89 for hyper-sn and 0.77 for smooth-sn, whereas bursty-sn has a higher average of

1.31. For bursty-sn, the average  $\sigma_{\text{UV}}^{\text{dust}}$  increases with decreasing mass bin, ranging from 1.07 to 1.47, with a significant fraction of objects having  $\sigma_{\text{UV}}^{\text{dust}} > 1.5$ . The maximum value reached in smooth-sn is  $\sigma_{\text{UV}}^{\text{dust}} = 1.5$ , with the average  $\sigma_{\text{UV}}^{\text{dust}}$  increasing from 0.57 to 1.1 from higher to lower halo mass bins. The hyper-sn model falls in-between the other two with average  $\sigma_{\text{UV}}^{\text{dust}}$  values ranging from 0.59 to 1.12.

In Figure 9 we show the median  $\sigma_{\text{UV}}^{\text{dust}}$  as a function of  $M_{\text{halo}}$ , where the former is calculated as the median value in each individual mass bin from all the curves corresponding to different redshift bins in Figure 7. We find that the median curves in all models exhibit a similar slope, confirming that lower mass halos are more sensitive to feedback effects, producing more fluctuations compared to massive halos. This is primarily due to the shallower potential wells of lower mass halos, which facilitate repeated cycles of inflow, star formation, and outflow (Gelli et al. 2020; Stern et al. 2021; Furlanetto & Mirocha 2022; Legrand et al. 2022; Gurvich et al. 2023; Byrne et al. 2023; Hopkins et al. 2023). Among the models, bursty-sn consistently produces the highest values. Additionally, the scatter around the median differs among the models, and, as expected, the bursty-sn model shows the largest scatter because of the wider range of variability in UVLF, while smooth-sn has the smallest. We also note that the slope of our curves is consistent with the one from the analytical fit by Gelli et al. (2024) based on the results of the FIRE-2 simulation at  $z \approx 8$  (Sun et al. 2023b), although the amplitude is matched only by the bursty-sn model.

Finally, in Figure 10 we show the redshift evolution of the average UV luminosity scatter ( $\sigma_{\text{UV}}^{\text{dust}}$ ) in different halo mass bins (at all redshifts), as well as computed over the full sample. We observe that

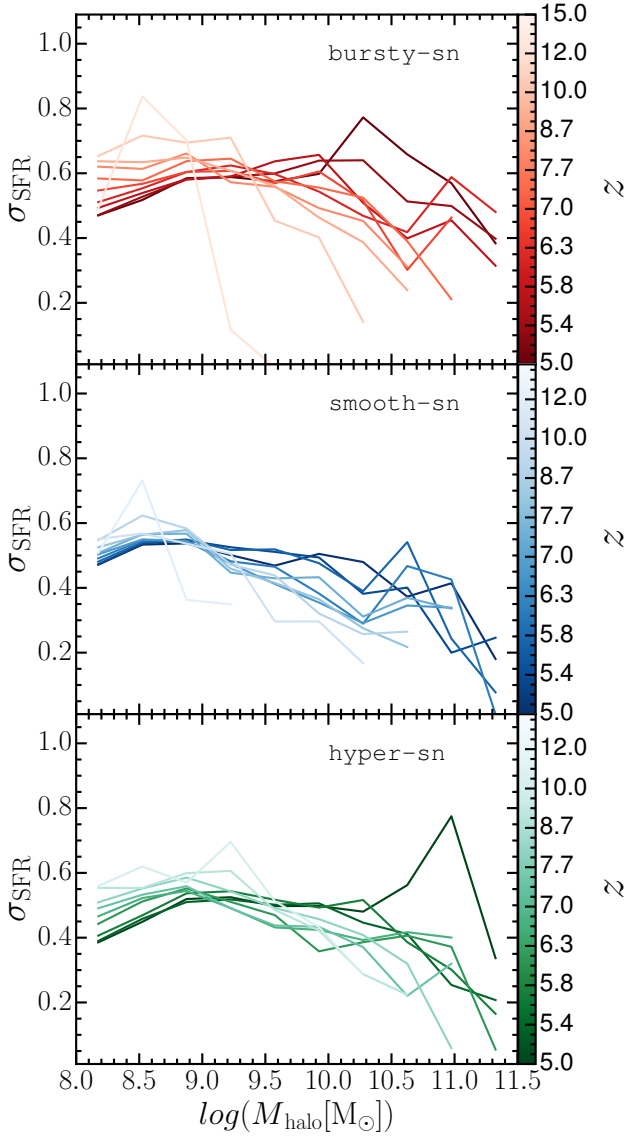


**Figure 5.**  $\sigma_{\text{SFR}}$  as a function of halo mass  $M_{\text{halo}}$  at different redshifts (indicated by the colorbar) for bursty-sn (top panel), smooth-sn (middle) and hyper-sn (bottom).

in all models  $\langle \sigma_{\text{UV}}^{\text{dust}} \rangle$  is largest for smaller halos, consistently with Figure 9. The curves for both the smooth-sn and hyper-sn models exhibit a clear and consistent trend across redshifts, with  $\langle \sigma_{\text{UV}}^{\text{dust}} \rangle$  generally decreasing with decreasing redshift with an exception at the highest halo mass bin where the scatter in UV luminosity remains roughly constant. In contrast, across all masses and redshifts, the bursty-sn model consistently exhibits the highest  $\langle \sigma_{\text{UV}}^{\text{dust}} \rangle$ , indicating more pronounced fluctuations in UVLF compared to the other models. Similarly to the trend observed in Figure 7, also here we see that in the bursty-sn model, as the UVLF variability increases rapidly below  $z \approx 10$ , has a peak of  $\langle \sigma_{\text{UV}}^{\text{dust}} \rangle \approx 2$  at  $z \approx 6.3$ , and then it drops sharply. Since the halo assembly history is similar in all models, this behaviour is unlikely to be driven solely by halo mass evolution. For example, its origin may also be connected to galaxy morphology, gas accretion history, level of turbulence in the ISM, and the rise of a UVB, as around this time the reionization process begins to accelerate for the bursty-sn model. This will be addressed

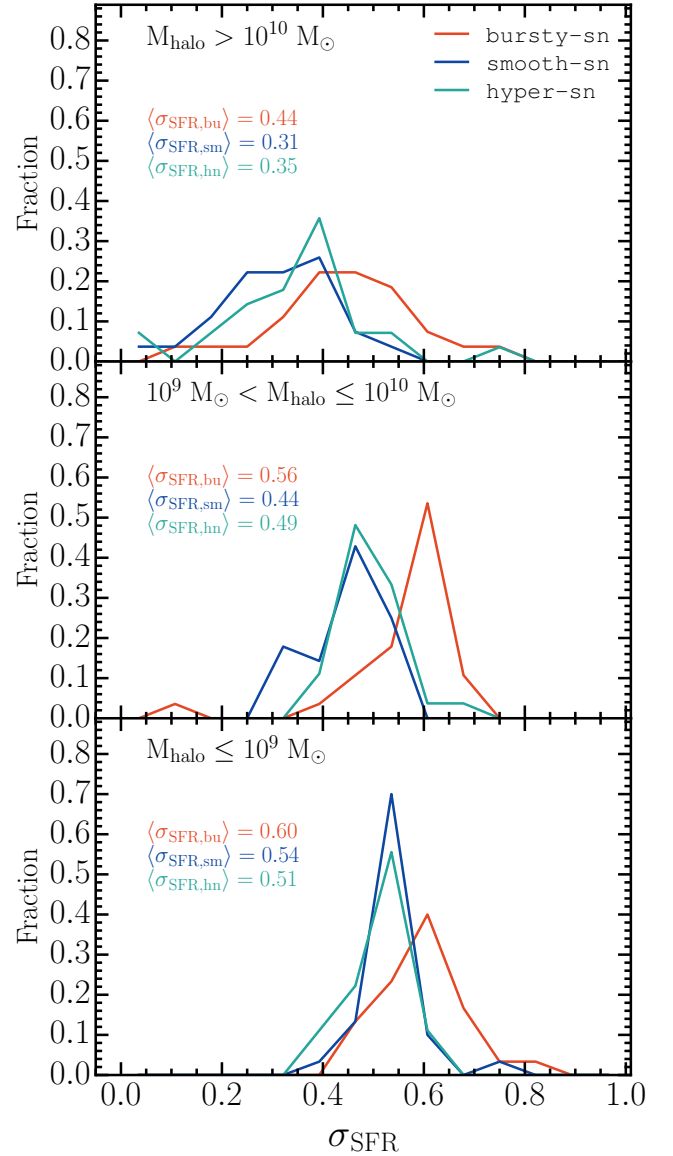


**Figure 6.** Distribution of  $\sigma_{\text{SFR}}$  in different  $M_{\text{halo}}$  bins for the three SN feedback models, as indicated by the colors. Numbers refer to the corresponding average standard deviation.

in more detail in a future study. Notably, at  $z \gtrsim 10$  for halos with  $M_{\text{halo}} > 10^9 M_{\odot}$ , hyper-sn produces the highest variability among all three models because of the impact of the stronger HN explosions dominating at that time.

We compare the results from the SPICE simulations to values extracted from observational (Ciesla et al. 2024; Endsley et al. 2024), as well as theoretical (Muñoz et al. 2023; Mason et al. 2023; Shen et al. 2023; Pallottini & Ferrara 2023; Sun et al. 2023b,a, 2024; Kravtsov & Belokurov 2024; Semenov et al. 2024) studies. Employing a semi-empirical approach, Muñoz et al. (2023) found a value of  $\langle \sigma_{\text{UV}}^{\text{dust}} \rangle$  as high as 2.5 at  $z \approx 12$ , which drops to 0.8 at  $z \leq 10$ . While none of our models reproduces such large high- $z$  values, at lower redshift there is a better agreement, although in this case our  $\langle \sigma_{\text{UV}}^{\text{dust}} \rangle$  are always slightly larger. Mason et al. (2023) utilized a fully empirical framework to predict that a  $\langle \sigma_{\text{UV}}^{\text{dust}} \rangle$  up to 1.5 in the range  $8 < z < 10$  is necessary for models to align with existing observations. These

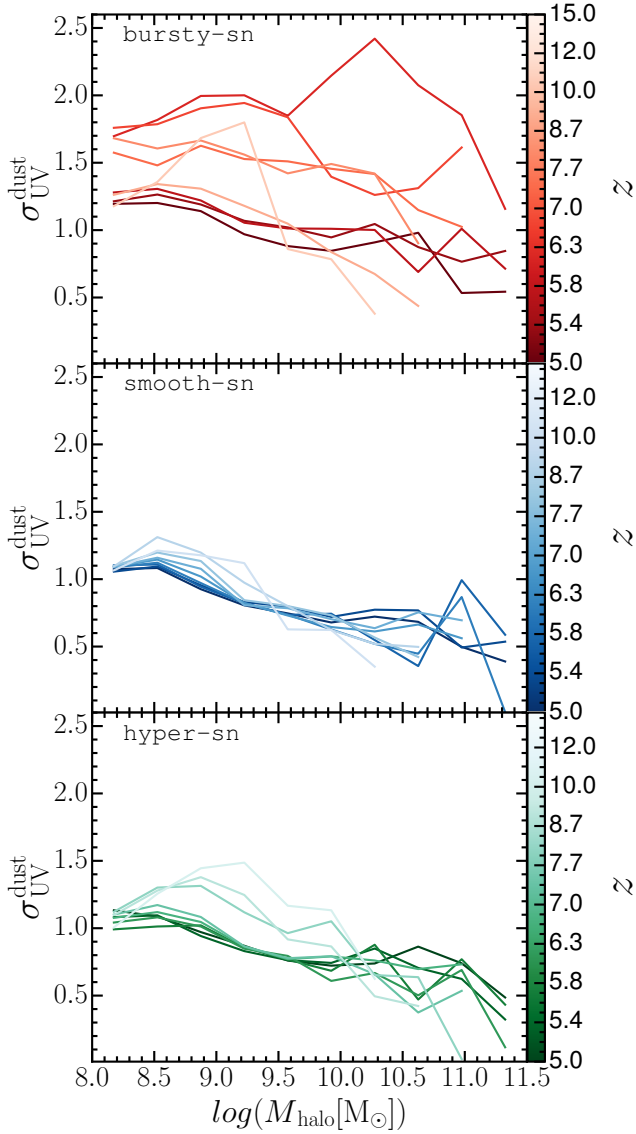


**Figure 7.**  $\sigma_{UV}^{\text{dust}}$  as a function of halo mass  $M_{\text{halo}}$  at different redshifts (indicated by the colorbar) for bursty-sn (top panel), smooth-sn (middle) and hyper-sn (bottom).

numbers are similar to those predicted in our bursty-sn model. Following a similar methodology, Shen et al. (2023) found a lower value of 0.75 at  $z \approx 9$ , which is instead consistent with those predicted by the smooth-sn and hyper-sn models. At  $z \approx 10$  and 12, though, they predict values of 1.5 and 2.0, respectively, which are higher than those of our models. Using a semi-analytical approach, Sun et al. (2024) (but see also Sun et al. 2023a,b, where bursty star formation in FIRE-2 simulation has been used to explain high redshift JWST observations) found the most probable UVLF variability value to be  $\approx 1.9 \pm 1.0$  at  $z \approx 6$ . At the same redshift, Endsley et al. (2024) found a variability in the range 1-2, obtained by analyzing Lyman-break galaxies assembled from ACS+NIRCam imaging in the GOODS and Abell 2744 fields. These values are generally reproduced in bursty-sn, as well as by halos with  $M_{\text{halo}} \leq 10^9 M_{\odot}$  in the other models. Ciesla et al. (2024), using spectral energy distribution modeling with the CIGALE code, and assuming a non-parametric star formation history on the JADES public catalog, found  $\langle \sigma_{UV}^{\text{dust}} \rangle \sim 1.2$

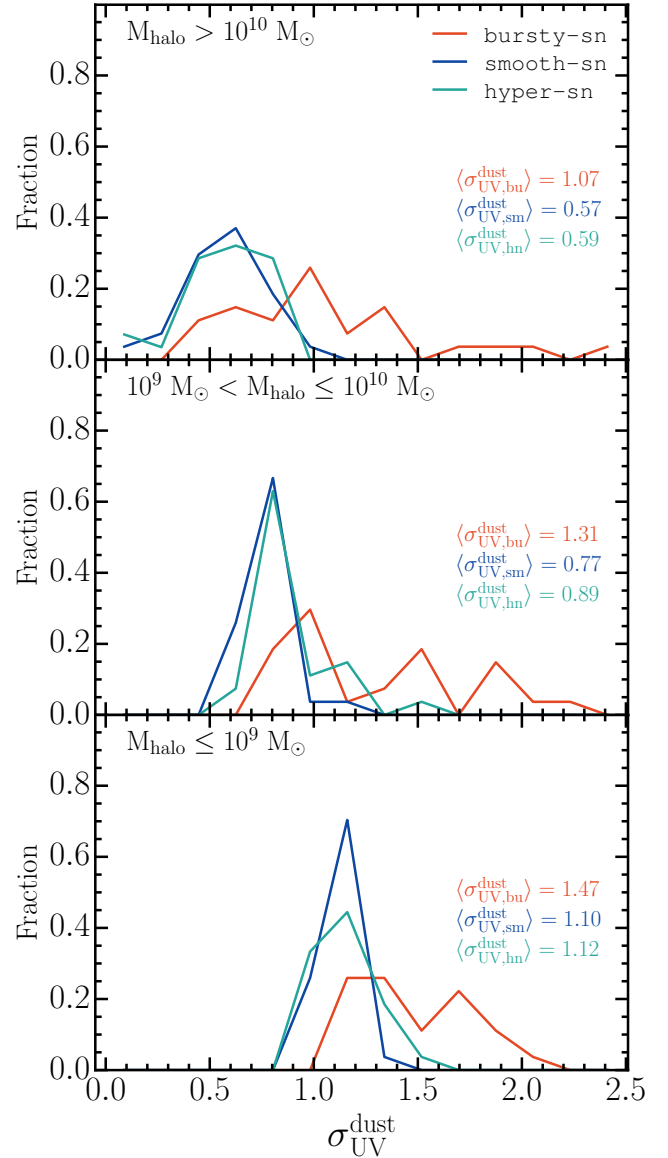


**Figure 8.** Distribution of  $\sigma_{UV}^{\text{dust}}$  in different  $M_{\text{halo}}$  bins for the three SN feedback models, as indicated by the colors. Numbers refer to the corresponding average standard deviation.

in the range  $6.5 < z < 10.5$ , which is fairly consistent with our bursty-sn model. Pallottini & Ferrara (2023) analyzed 245 galaxies from the SERRA simulation suite at  $z \approx 7.7$ , finding a  $\langle \sigma_{UV}^{\text{dust}} \rangle$  of 0.61. We note, though, that the method employed for this evaluation differs from that used in our study and other works (see appendix A for more details). Finally, Semenov et al. (2024) investigated the importance of turbulent star formation by utilizing detailed modelling of cold turbulent ISM, star formation and feedback through zoom-in high resolution simulation of an early forming Milky Way analog, and they found that the variability decreases with time, similarly to the predictions of our models, with the exception of the  $6 < z < 9$  range in bursty-sn. It is also interesting to note that the curves for the smooth-sn and hyper-sn models in the lowest mass bin aligns very well with Semenov et al. (2024) till  $z \approx 7.5$ , whereas after that the latter shows much lower values.

In general, we can conclude that the constraints from observational



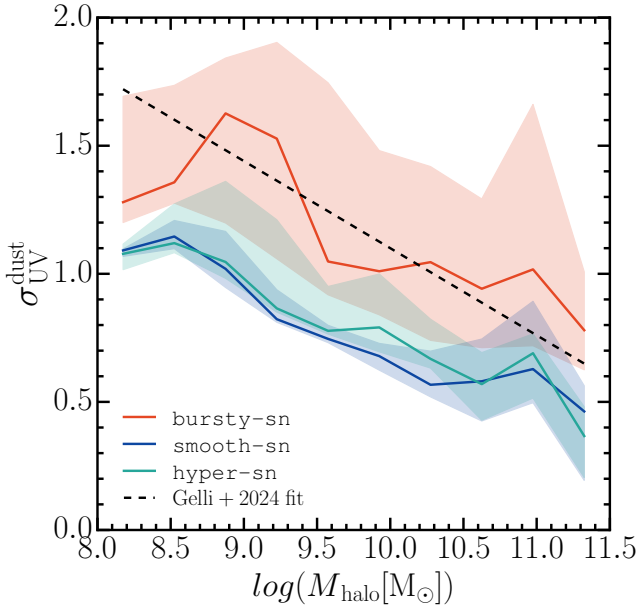


**Figure 9.** Dependence of  $\sigma_{UV}^{dust}$  on the DM halo mass  $M_{halo}$ . The solid curves refer to the median value, while the shaded regions are the standard deviation. Colors refer to the different SN feedback models, while the black dashed curve represents the fit from Gelli et al. (2024).

and other theoretical models can not specifically distinguish between the SN feedback models in SPICE due to their large scatter in  $\sigma_{UV}^{dust}$  across different redshifts.

#### 4 CONCLUSIONS

In this study we investigate the role played by SN feedback in driving the variability of the UVLF using the suite of radiation-hydrodynamic simulations SPICE. This includes three models for SN feedback, which differ in terms of explosion energy and timing. The *bursty-sn* model, characterized by intense and episodic supernova explosions, shows the highest SFR variability, leading to significant fluctuations in UV luminosity. The *smooth-sn* model, in which energy injection happens more continuously and thus the effect of feedback is less disruptive, produces a higher and less variable SFR, resulting also in a lower UVLF variability. The *hyper-sn* model shows an intermediate trend, with higher variability at early times due to HN effects, and a behaviour similar to the one of *smooth-sn* at lower redshifts, when the fraction of HN events decreases. Our main findings can be summarized as follows:

- The good agreement between all models and the observed UV luminosity functions discussed in Bhagwat et al. (2024) is obtained even at the highest redshifts analyzed here, i.e.  $z \approx 11$  and 12.
- We find that not only the most massive objects contribute to the bright end of the LF, i.e. with dust corrected magnitude  $M_{UV}^{dust} \leq -17$ , but also those with  $M_* \sim 10^{(6.5-7)} M_{\odot}$  can be a very bright object detected by JWST. The median stellar mass of these bright objects in our models is consistent with those derived by Mason et al. (2015, 2023) at all redshifts.
- The nature of SN feedback has a significant impact on the temporal evolution of the UVLF, as we show for time intervals of 10, 30, and 50 Myr at  $z \approx 10$  and 8. The *bursty-sn* model produces the

highest UVLF fluctuations, with a deviation of more than 1 dex. In comparison, the evolution of the UVLF in *smooth-sn* and *hyper-sn* is more gradual, with the latter having much higher fluctuations than the former at  $z \approx 10$ .

- The burstiness of star formation and UVLF is strongly influenced by the SN feedback, with the *bursty-sn* and *smooth-sn* models consistently exhibiting the highest and lowest variability, respectively. The disruptive nature of the *bursty-sn* model leads to both higher median values and larger scatter in  $\sigma_{UV}^{dust}$ , indicating stronger fluctuations in dust-obscured UV emission. In contrast, the *hyper-sn* model displays an intermediate behavior, balancing between the extremes of the other two models.

- All models show a similar dependence of the SFR and UVLF variability on the halo mass, with the extent of the fluctuations being higher for the lowest mass haloes, which are more susceptible to feedback effects. We find that the median  $\sigma_{UV}^{dust}$  as a function of  $M_{halo}$  in all models exhibit a similar slope, consistent with the one from the analytical fit from the FIRE-2 simulation at  $z \approx 8$  by Sun et al. (2023b), although the amplitude is matched only by the *bursty-sn* model.

- The redshift dependence of the average standard deviation  $\langle \sigma_{UV}^{dust} \rangle$  is similar in *smooth-sn* and *hyper-sn*, with a variability which remains almost constant, although in the latter model it is slightly higher. In contrast, the *bursty-sn* model shows an increase in  $\langle \sigma_{UV}^{dust} \rangle$  from  $z \approx 10$  to  $\approx 6$ , before declining. Additionally, the *bursty-sn* model consistently exhibits the highest values of  $\langle \sigma_{UV}^{dust} \rangle$  across all masses and redshifts.

- We achieve the maximum UVLF variability as  $\sigma_{UV}^{dust} \sim 2.5$  in the *bursty-sn* model. Conversely, the smoother star formation history typical of the *smooth-sn* model fails to induce a large variability, with values of  $\sigma_{UV}^{dust}$  below 1.3. The *hyper-sn* model lies in between the other two, although its characteristics are more similar to those of the *smooth-sn* one, with  $\sigma_{UV}^{dust}$  extending up to 1.5.

This work emphasizes the critical role of SN feedback in shaping the variability of the UVLF. While our study suggests that SN feedback is the primary mechanism influencing the UVLF variability, the observed features arise from a complex interplay of multiple factors (i.e. UVB, gas accretion history, ISM turbulence) that requires further detailed investigation. Here, though, we provide new insights into how variations in feedback strength and timing impact the burstiness of star formation and UV emission, and we emphasize the importance of explaining how the variability depends on both mass and redshift, an aspect often overlooked in prior studies. Our investigation also suggests the UVLF variability may alleviate the bright galaxy tension observed by JWST at high redshifts.

#### ACKNOWLEDGEMENTS

All the analysis were carried out on the machines of Max Planck Institute for Astrophysics (MPA) and Max Planck Computing and Data Facility (MPCDF). AB thanks the entire EoR research group of MPA for all the encouraging comments for this project. This work made extensive use of publicly available software packages : `numpy` (van der Walt et al. 2011), `matplotlib` (Hunter 2007), `scipy` (Jones et al. 2001). Authors thank the developers of these packages.

#### DATA AVAILABILITY

The final data products from this study will be shared on reasonable request to the authors.

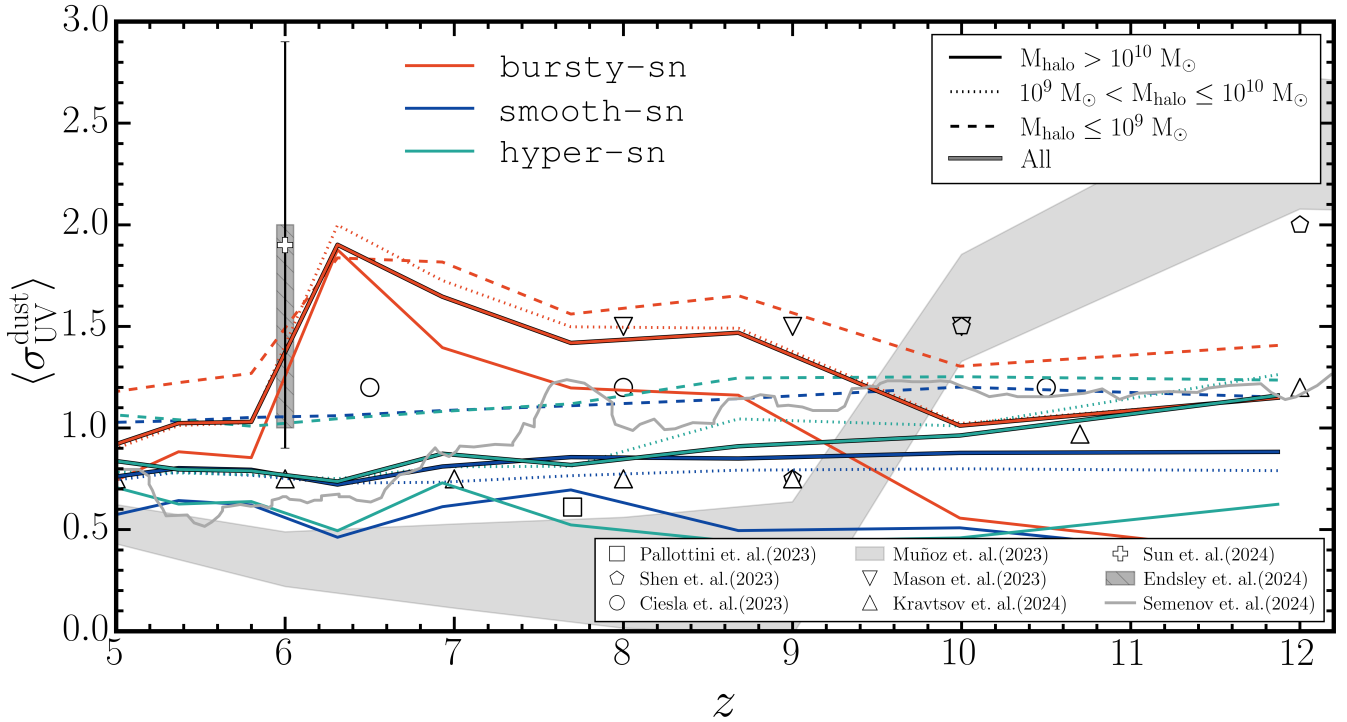


**Figure 10.** Redshift evolution of  $\langle \sigma_{UV}^{dust} \rangle$  for  $M_{halo} < 10^9 M_{\odot}$  (dashed lines),  $10^9 M_{\odot} < M_{halo} < 10^{10} M_{\odot}$  (dotted) and  $M_{halo} > 10^{10} M_{\odot}$  (solid). The curves for the entire sample are shown in solid curve with black edges. Colors refer to the three SN feedback models, while the values from observational and other theoretical studies (Pallottini & Ferrara 2023; Shen et al. 2023; Ciesla et al. 2024; Muñoz et al. 2023; Mason et al. 2023; Kravtsov & Belokurov 2024; Sun et al. 2024; Endsley et al. 2024; Semenov et al. 2024) are shown in grey data points and shaded regions.

## REFERENCES

- Acharya A., et al., 2024, [arXiv e-prints](#), p. [arXiv:2410.11620](#)
- Adams N. J., et al., 2023, *MNRAS*, **518**, 4755
- Alexandroff R. M., Heckman T. M., Borthakur S., Overzier R., Leitherer C., 2015, *ApJ*, **810**, 104
- Anglés-Alcázar D., Faucher-Giguère C.-A., Kereš D., Hopkins P. F., Quataert E., Murray N., 2017, *MNRAS*, **470**, 4698
- Aoyama S., Hou K.-C., Hirashita H., Nagamine K., Shimizu I., 2018, *MNRAS*, **478**, 4905
- Atek H., et al., 2023, *MNRAS*, **519**, 1201
- Bagley M. B., et al., 2022, [arXiv e-prints](#), p. [arXiv:2205.12980](#)
- Bhagwat A., Costa T., Ciardi B., Pakmor R., Garaldi E., 2024, *MNRAS*, **523**, 3201
- Biagetti M., Franciolini G., Riotto A., 2023, *ApJ*, **944**, 113
- Bird S., Chang C.-F., Cui Y., Yang D., 2023, [arXiv e-prints](#), p. [arXiv:2307.10302](#)
- Bournaud F., Elmegreen B. G., Elmegreen D. M., 2007, *ApJ*, **670**, 237
- Bouwens R. J., et al., 2015, *ApJ*, **803**, 34
- Bouwens R., Illingworth G., Oesch P., Stefanon M., Naidu R., van Leeuwen I., Magee D., 2023a, *MNRAS*, **523**, 1009
- Bouwens R. J., et al., 2023b, *MNRAS*, **523**, 1036
- Bowler R. A. A., Jarvis M. J., Dunlop J. S., McLure R. J., McLeod D. J., Adams N. J., Milvang-Jensen B., McCracken H. J., 2020, *MNRAS*, **493**, 2059
- Boylan-Kolchin M., 2023, *Nature Astronomy*, **7**, 731
- Byrne L., Faucher-Giguère C.-A., Stern J., Anglés-Alcázar D., Wellons S., Gurvich A. B., Hopkins P. F., 2023, *MNRAS*, **520**, 722
- Casey C. M., et al., 2024, *ApJ*, **965**, 98
- Castellano M., et al., 2022, *ApJ*, **938**, L15
- Ceverino D., Dekel A., Bournaud F., 2010, *MNRAS*, **404**, 2151
- Chabrier G., 2003, *PASP*, **115**, 763
- Chon S., Hosokawa T., Omukai K., Schneider R., 2024, *MNRAS*, **530**, 2453
- Ciardi B., Bianchi S., Ferrara A., 2002, *MNRAS*, **331**, 463
- Ciesla L., et al., 2024, *A&A*, **686**, A128
- Coe D., et al., 2013, *ApJ*, **762**, 32
- Contini M., Contini T., 2003, *MNRAS*, **342**, 299
- Cueto E. R., Hutter A., Dayal P., Gottlöber S., Heintz K. E., Mason C., Trebitsch M., Yepes G., 2024, *A&A*, **686**, A138
- Dayal P., Giri S. K., 2023, [arXiv e-prints](#), p. [arXiv:2303.14239](#)
- Dekel A., Sari R., Ceverino D., 2009, *ApJ*, **703**, 785
- Dekel A., Sarkar K. C., Birnboim Y., Mandelker N., Li Z., 2023, *MNRAS*, **523**, 3201
- Díaz-Rodríguez M., Murphy J. W., Rubin D. A., Dolphin A. E., Williams B. F., Dalcanton J. J., 2018, *ApJ*, **861**, 92
- Díaz-Rodríguez M., Murphy J. W., Williams B. F., Dalcanton J. J., Dolphin A. E., 2021, *MNRAS*, **506**, 781
- Donnan C. T., et al., 2023a, *MNRAS*, **518**, 6011
- Donnan C. T., et al., 2023b, *MNRAS*, **518**, 6011
- Donnan C. T., McLeod D. J., McLure R. J., Dunlop J. S., Carnall A. C., Cullen F., Magee D., 2023c, *MNRAS*, **520**, 4554
- Donnan C. T., et al., 2024, [arXiv e-prints](#), p. [arXiv:2403.03171](#)
- El-Badry K., Wetzel A., Geha M., Hopkins P. F., Kereš D., Chan T. K., Faucher-Giguère C.-A., 2016, *ApJ*, **820**, 131
- Eldridge J. J., Stanway E. R., Xiao L., McClelland L. A. S., Taylor G., Ng M., Greis S. M. L., Bray J. C., 2017, *Publ. Astron. Soc. Australia*, **34**, e058
- Elmegreen B. G., Elmegreen D. M., Fernandez M. X., Lomonias J. J., 2009, *ApJ*, **692**, 12
- Emami N., Siana B., Weisz D. R., Johnson B. D., Ma X., El-Badry K., 2019, *ApJ*, **881**, 71
- Endsley R., Chisholm J., Stark D. P., Topping M. W., Whittler L., 2024, [arXiv e-prints](#), p. [arXiv:2410.01905](#)
- Esmerian C. J., Gnedin N. Y., 2024, *ApJ*, **968**, 113
- Faucher-Giguère C.-A., 2018, *MNRAS*, **473**, 3717
- Ferrara A., Pallottini A., Dayal P., 2023, *MNRAS*, **522**, 3986

- Ferrara A., Carniani S., di Mascia F., Bouwens R., Oesch P., Schouws S., 2024, ALMA observations of super-early galaxies: attenuation-free model predictions (arXiv:2409.17223), <https://arxiv.org/abs/2409.17223>
- Finkelstein S. L., et al., 2022, *ApJ*, 940, L55
- Fiore F., Ferrara A., Bischetti M., Feruglio C., Travascio A., 2023, *The Astrophysical Journal Letters*, 943, L27
- Flores Velázquez J. A., et al., 2021, *MNRAS*, 501, 4812
- Förster Schreiber N. M., Shapley A. E., Erb D. K., Genzel R., Steidel C. C., Bouché N., Cresci G., Davies R., 2011, *ApJ*, 731, 65
- Fukushima H., Yajima H., 2022, *MNRAS*, 511, 3346
- Furlanetto S. R., Mirocha J., 2022, *MNRAS*, 511, 3895
- Gelli V., Salvadori S., Pallottini A., Ferrara A., 2020, *MNRAS*, 498, 4134
- Gelli V., Mason C., Hayward C. C., 2024, arXiv e-prints, p. arXiv:2405.13108
- Gong Y., Yue B., Cao Y., Chen X., 2023, *ApJ*, 947, 28
- Guillet T., Teyssier R., 2011, *Journal of Computational Physics*, 230, 4756
- Gurvich A. B., et al., 2023, *MNRAS*, 519, 2598
- Harikane Y., et al., 2022, *ApJS*, 259, 20
- Harikane Y., et al., 2023, *ApJS*, 265, 5
- Harper D. A., Low F. J., 1971, *ApJ*, 165, L9
- Haskell P., Das S., Smith D. J. B., Cochrane R. K., Hayward C. C., Anglés-Alcázar D., 2024, *MNRAS*, 530, L7
- Heckman T. M., Sembach K. R., Meurer G. R., Leitherer C., Calzetti D., Martin C. L., 2001, *ApJ*, 558, 56
- Helton J. M., et al., 2024, arXiv e-prints, p. arXiv:2405.18462
- Hirano S., Yoshida N., 2023, arXiv e-prints, p. arXiv:2306.11993
- Hollis M., 2023, *Nature Astronomy*, 7, 885
- Hopkins P. F., et al., 2023, *MNRAS*,
- Hunter J. D., 2007, *Computing in Science and Engineering*, 9, 90
- Hutter A., Cueto E. R., Dayal P., Gottlöber S., Trebitsch M., Yepes G., 2024, arXiv e-prints, p. arXiv:2410.00730
- Inayoshi K., Harikane Y., Inoue A. K., Li W., Ho L. C., 2022, *ApJ*, 938, L10
- Iyer K. G., et al., 2020, *MNRAS*, 498, 430
- Jain S., Tacchella S., Mosleh M., 2024, *MNRAS*, 527, 3291
- Jones E., Oliphant T., Peterson P., 2001
- Kimm T., Cen R., Devriendt J., Dubois Y., Slyz A., 2015, Towards simulating star formation in turbulent high- $z$  galaxies with mechanical supernova feedback (arXiv:1501.05655)
- Kravtsov A., Belokurov V., 2024, arXiv e-prints, p. arXiv:2405.04578
- Kretschmer M., Teyssier R., 2020, *MNRAS*, 492, 1385
- Larsen P., Sommer-Larsen J., Andersen A. C., 2009, *ApJ*, 704, 1640
- Legrand L., Hutter A., Dayal P., Ucci G., Gottlöber S., Yepes G., 2022, *MNRAS*, 509, 595
- Leung G. C. K., et al., 2023, *ApJ*, 954, L46
- Lovell C. C., Harrison I., Harikane Y., Tacchella S., Wilkins S. M., 2023, *MNRAS*, 518, 2511
- Lower S., Narayanan D., Leja J., Johnson B. D., Conroy C., Davé R., 2020, *ApJ*, 904, 33
- Luberto J., Furlanetto S., Mirocha J., 2024, arXiv e-prints, p. arXiv:2409.20519
- Mason C. A., Trenti M., Treu T., 2015, *ApJ*, 813, 21
- Mason C. A., Trenti M., Treu T., 2023, *MNRAS*, 521, 497
- McLeod D. J., et al., 2024, *MNRAS*, 527, 5004
- Michel-Dansac L., Blaizot J., Garel T., Verhamme A., Kimm T., Trebitsch M., 2020, *A&A*, 635, A154
- Mirocha J., Furlanetto S. R., 2023, *MNRAS*, 519, 843
- Morishita T., Stiavelli M., 2023, *ApJ*, 946, L35
- Morishita T., et al., 2018, *ApJ*, 867, 150
- Muñoz J. B., Mirocha J., Furlanetto S., Sabti N., 2023, *MNRAS*, 526, L47
- Naidu R. P., et al., 2022, *ApJ*, 940, L14
- Narayanan D., et al., 2024, *ApJ*, 961, 73
- Nguyen B., Pacucci F., Carniani S., Maiolino R., Fan X., 2024, in *American Astronomical Society Meeting Abstracts*. p. 307.03
- Nickerson S., Teyssier R., Rosdahl J., 2018, *Monthly Notices of the Royal Astronomical Society*, 479, 3206–3226
- Ocvirk P., et al., 2024, arXiv e-prints, p. arXiv:2409.05946
- Oesch P. A., et al., 2016, *ApJ*, 819, 129
- Padmanabhan H., Loeb A., 2023, *ApJ*, 953, L4
- Pallottini A., Ferrara A., 2023, *A&A*, 677, L4
- Parashari P., Laha R., 2023, *MNRAS*,
- Pérez-González P. G., et al., 2023, *ApJ*, 951, L1
- Planck Collaboration et al., 2016, *A&A*, 594, A13
- Robertson B., et al., 2024, *ApJ*, 970, 31
- Rosdahl J., Teyssier R., 2015, *MNRAS*, 449, 4380
- Rosdahl J., Blaizot J., Aubert D., Stranex T., Teyssier R., 2013, *MNRAS*, 436, 2188
- Sabti N., Muñoz J. B., Kamionkowski M., 2023, arXiv e-prints, p. arXiv:2305.07049
- Schechter P., 1976, *ApJ*, 203, 297
- Semenov V. A., Conroy C., Hernquist L., 2024, arXiv e-prints, p. arXiv:2410.09205
- Shen X., Vogelsberger M., Boylan-Kolchin M., Tacchella S., Kannan R., 2023, *MNRAS*, 525, 3254
- Smit R., Bouwens R. J., Labbé I., Franx M., Wilkins S. M., Oesch P. A., 2016, *ApJ*, 833, 254
- Sparre M., Hayward C. C., Feldmann R., Faucher-Giguère C.-A., Muratov A. L., Kereš D., Hopkins P. F., 2017, *MNRAS*, 466, 88
- Stanway E. R., Eldridge J. J., 2018, *MNRAS*, 479, 75
- Steinhardt C. L., Kokorev V., Rusakov V., Garcia E., Sneppen A., 2023, *ApJ*, 951, L40
- Stern J., et al., 2021, *ApJ*, 911, 88
- Sukhbold T., Ertl T., Woosley S. E., Brown J. M., Janka H. T., 2016, *ApJ*, 821, 38
- Sun G., Faucher-Giguère C.-A., Hayward C. C., Shen X., 2023a, *MNRAS*, 526, 2665
- Sun G., Faucher-Giguère C.-A., Hayward C. C., Shen X., Wetzel A., Cochrane R. K., 2023b, *ApJ*, 955, L35
- Sun G., Muñoz J. B., Mirocha J., Faucher-Giguère C.-A., 2024, arXiv e-prints, p. arXiv:2410.21409
- Tacchella S., Dekel A., Carollo C. M., Ceverino D., DeGraf C., Lapiner S., Mandelker N., Primack Joel R., 2016, *MNRAS*, 457, 2790
- Tacchella S., Forbes J. C., Caplar N., 2020, *MNRAS*, 497, 698
- Teyssier R., 2002, *A&A*, 385, 337
- Treu T., et al., 2023, *ApJ*, 942, L28
- Whitler L., Stark D. P., Endsley R., Chen Z., Mason C., Topping M. W., Charlot S., 2024, *MNRAS*, 529, 855
- Whitler L., et al., 2025, arXiv e-prints, p. arXiv:2501.00984
- Willott C. J., et al., 2024, *ApJ*, 966, 74
- Yung L. Y. A., Somerville R. S., Finkelstein S. L., Wilkins S. M., Gardner J. P., 2023, arXiv e-prints, p. arXiv:2304.04348
- Zhao R. J., Furlanetto S. R., 2024, *J. Cosmology Astropart. Phys.*, 2024, 018
- Zheng W., et al., 2012, *Nature*, 489, 406
- van der Walt S., Colbert S. C., Varoquaux G., 2011, *Computing in Science and Engineering*, 13, 22

## APPENDIX A: COMPARISON BETWEEN DIFFERENT METHODS FOR COMPUTING $\sigma_{UV}$

In this section, we discuss how our major findings are affected by adopting the method proposed by Pallottini & Ferrara (2023) (hereafter referred to as PF23) in the calculation of the variability. We begin by analyzing the temporal evolution of the SFR for the most massive halo at  $z = 5$  illustrated in Figure 4. Each curve is fitted with a third-order polynomial on a log-linear scale (i.e.  $SFR_{fit}$ ), following the technique used by PF23. The stochastic variability of the SFR is then quantified by computing the residuals, defined as  $\delta_{SFR} = \log_{10}(SFR/SFR_{fit})$ , from which we derive the standard deviation,  $\sigma_{SFR}$ . The results of this approach are compared with the standard method presented in Section 3.2 and summarized in Figure A1. We observe that the  $\delta_{SFR}$  distribution using the PF23 method is slightly shifted toward higher values across all models compared to the standard method. This shift is reflected in the slightly higher values of  $\sigma_{SFR}$ , with 0.39 for bursty-sn, 0.17 for smooth-sn, and

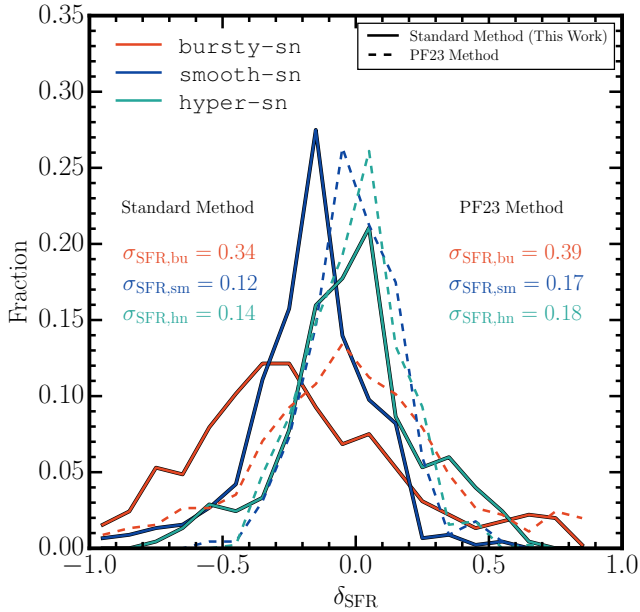


**Figure A1.** Distribution of  $\delta_{\text{SFR}}$  computed from the temporal evolution of the most massive halo at  $z = 5$  as shown in Figure 4. Colors refer to different SN feedback models. The solid and dashed curves represent the results obtained using the standard method and those from the method proposed by Pallottini & Ferrara (2023). Numbers refer to the corresponding standard deviation.

0.19 for hyper-sn, each exceeding the standard method’s results by approximately  $\Delta(\sigma_{\text{SFR}}) \sim 0.04 - 0.05$ . To examine the behavior of the entire halo population at  $z = 5$ , Figure A2 presents the distribution of  $\sigma_{\text{SFR}}$  calculated using both methods across all SN feedback models. Interestingly, we observe that the PF23 method yields a distribution of  $\sigma_{\text{SFR}}$  values that are slightly lower across all models when compared to the standard method. This finding contrasts with the trend seen in Figure A1. Specifically, we note that the peak of the  $\sigma_{\text{SFR}}$  distribution shifts by approximately 0.15 – 0.2.

The key difference lies in the PF23 method’s focus on the temporal evolution of individual halos up to the redshift of interest, which emphasizes fluctuations around the median evaluated for the same halo, differently from other methods which calculate the median from the full sample of halos. This distinction leads to a fundamentally different interpretation of the underlying variability being measured, with the PF23 method offering a more detailed view of individual halo evolution over time.

## APPENDIX B: FITTING AND EXTRAPOLATION OF UVLF

To investigate whether the SPICE UVLF, incorporating scatter, can effectively reproduce the observed luminosity functions, we fit each UVLF with a Schechter (1976) function<sup>2</sup>. In Table B1, we show the fitted parameters for  $z = 5, 6, 7, 9, 10, 12$ . We note that for  $M_{\text{UV}} \lesssim -19$ , SPICE lacks a sufficient statistical sample of halos for a robust fitting. As a result, the Schechter function fails to provide an

<sup>2</sup> The functional form is given by :  

$$\Phi(M_{\text{UV}}) = 0.4 \ln(10) \phi^* \left[ 10^{0.4(M_{\text{UV}}^* - M_{\text{UV}})(\alpha+1)} \right] \exp \left[ -10^{0.4(M_{\text{UV}}^* - M_{\text{UV}})} \right],$$
where  $\phi^*$  is the normalization factor,  $M_{\text{UV}}^*$  is the characteristic magnitude and  $\alpha$  is the faint-end slope.

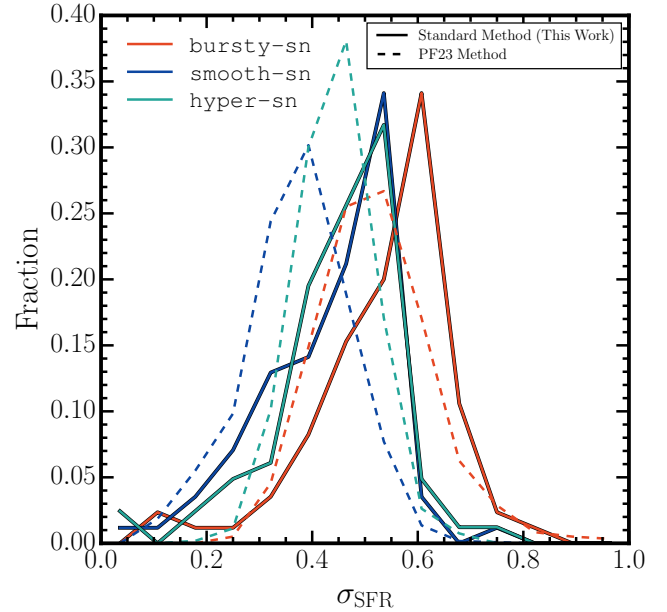


**Figure A2.** Distribution of  $\sigma_{\text{SFR}}$  computed over the entire sample of halos present at  $z = 5$ . Colors refer to different SN feedback models. Curves represent the two different methods as in Figure A1.

optimal fit, leading to progressively higher deviations from the SPICE LFs towards lower  $M_{\text{UV}}$  values relative to the fitted characteristic magnitude ( $M_{\text{UV}}^*$ ). Consequently, the reduced  $\chi^2$  values are notably low in some cases where the deviations are larger, particularly at higher redshifts.

As a reference, in Figure B1 we plot the fitted curves at  $z = 10$  and  $12$  as solid lines, while the shaded regions represent the  $2\text{-}\sigma$  scatter obtained by performing the fits for the curves corresponding to 10, 30, and 50 Myr before and after the reference redshift. As mentioned above, the fit at the brightest end of the LF is not robust, and indeed all models fall below observational data, although it has previously been noticed (Bowler et al. 2020; Donnan et al. 2024; Whittler et al. 2025) that high- $z$  galaxies with  $M_{\text{UV}} \lesssim -22$  are in excess of the exponential decline of the Schechter function. At both redshifts, the bursty-sn and smooth-sn models perform similarly in reproducing observations within the range  $-19 \lesssim M_{\text{UV}} \lesssim -17$ , with the latter exhibiting slightly smaller scatter. Both models align more closely with the data toward the brighter end, up to  $M_{\text{UV}} \approx -20$ , at  $z \approx 12$ . Beyond this point, they systematically underpredict the data, with deviations becoming progressively larger at lower  $M_{\text{UV}}$ . The hyper-sn model, while displaying a greater scatter in comparison to smooth-sn at  $z \approx 12$ , does not achieve better agreement with the data, instead showing a significant offset from observations. At  $z \approx 10$ , however, its predictions remain comparable to those of other models, with the lowest scatter observed. To provide additional information, we also include the  $2\text{-}\sigma$  scatter obtained by linearly extrapolating the SPICE UVLFs corresponding to 10, 30, and 50 Myr before and after the reference redshift beyond the  $M_{\text{UV}}$  range available in SPICE, without applying any fitting procedure. These curves align more closely with observations across the entire  $M_{\text{UV}}$  range, with hyper-sn offering the best overall agreement at both redshifts. The bursty-sn model tends to overpredict the counts at  $z \approx 12$ , but closely matches most observational constraints at  $z \approx 10$ . Conversely, smooth-sn



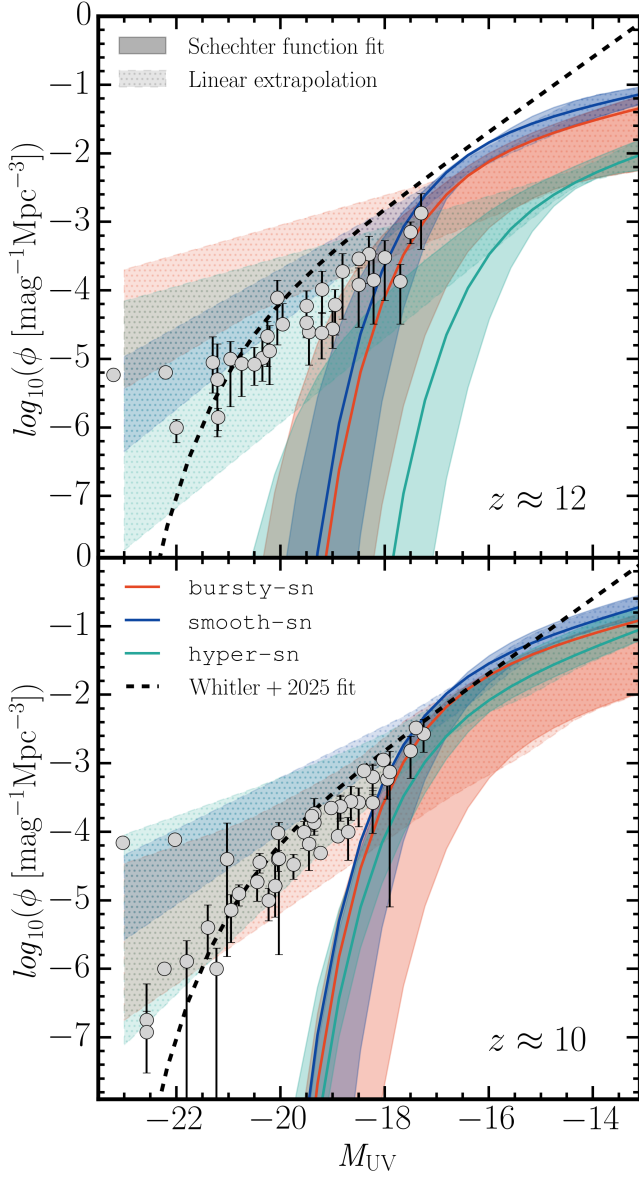


**Figure B1.** UVLF at  $z = 12$  (*top panel*) and  $10$  (*bottom*) obtained after fitting with a [Schechter \(1976\)](#) function (solid lines). Shaded regions represent the  $2\text{-}\sigma$  scatter calculated from the evolution of the UVLF over time intervals of 10, 30, and 50 Myr around the reference redshifts. The hatched shaded regions indicate a direct extrapolations of the UVLFs. Colors refer to different SN feedback models. The black dashed curve indicates the result from [Whittler et al. \(2025\)](#) fitted to their observational F115W dropout sample assuming a [Schechter \(1976\)](#) function, while a compilation of observations from HST and JWST ([Bouwens et al. 2015](#); [Harikane et al. 2022](#); [Naidu et al. 2022](#); [Adams et al. 2023](#); [Harikane et al. 2023](#); [Bouwens et al. 2023a,b](#); [Leung et al. 2023](#); [Donnan et al. 2023b,c](#); [Pérez-González et al. 2023](#); [Casey et al. 2024](#); [Robertson et al. 2024](#); [McLeod et al. 2024](#); [Whittler et al. 2025](#)) is shown as gray data points.

performs the worst overall, but shows better agreement at  $z \approx 12$  than at  $z \approx 10$ .

This paper has been typeset from a  $\text{\TeX}/\text{\LaTeX}$  file prepared by the author.

$z$	$\phi^* (\times 10^{-3})$			$M_{\text{UV}}^*$			$\alpha$			$\chi^2_{\nu}$		
	Bursty	Smooth	Hyper	Bursty	Smooth	Hyper	Bursty	Smooth	Hyper	Bursty	Smooth	Hyper
5	75.95	256.11	23.36	-17.32	-16.84	-17.81	-1.53	-1.40	-1.67	0.40	2.68	0.39
7	44.19	155.57	63.89	-17.12	-16.62	-16.93	-1.61	-1.45	-1.59	0.45	1.92	0.78
9	0.18	136.72	34.28	-19.96	-15.93	-16.53	-1.89	-1.39	-1.65	0.06	0.33	0.12
10	30.84	67.20	12.23	-16.51	-16.14	-16.51	-1.48	-1.48	-1.67	0.21	0.15	0.06
12	14.18	21.13	4.06	-16.38	-16.66	-15.22	-1.43	-1.42	-1.55	0.02	0.02	0.01

**Table B1.** Fitted parameters of the UVLF functional forms at various redshifts, modeled using the [Schechter \(1976\)](#) function. The parameters include the overall normalization ( $\phi^*$ ), the characteristic magnitude ( $M_{\text{UV}}^*$ ), and the faint-end slope ( $\alpha$ ). The reduced chi-square ( $\chi^2_{\nu}$ ) values assess the goodness of fit.